Yi et al. *Light: Science & Applications* (2023)12:106
https://doi.org/10.1038/s41377-023-01156-9

Official journal of the CIOMP 2047-7538
www.nature.com/lsa

ARTICLE Open Access

Bloch theorem dictated wave chaos in microcavity crystals

Chang-Hwan Yi[1], Hee Chul Park[1,2]✉ and Moon Jip Park[1,3]✉

Abstract

Universality class of wave chaos emerges in many areas of science, such as molecular dynamics, optics, and network theory. In this work, we generalize the wave chaos theory to cavity lattice systems by discovering the intrinsic coupling of the crystal momentum to the internal cavity dynamics. The *cavity-momentum locking* substitutes the role of the deformed boundary shape in the ordinary single microcavity problem, providing a new platform for the in situ study of microcavity light dynamics. The transmutation of wave chaos in periodic lattices leads to a phase space reconfiguration that induces a dynamical localization transition. The degenerate scar-mode spinors hybridize and non-trivially localize around regular islands in phase space. In addition, we find that the momentum coupling becomes maximal at the Brillouin zone boundary, so the intercavity chaotic modes coupling and wave confinement are significantly altered. Our work pioneers the study of intertwining wave chaos in periodic systems and provide useful applications in light dynamics control.

Introduction

Light dynamics in optical microcavity[1–6] provides the prominent platform to study quantum-classical correspondence, formally known as the field of quantum chaos[7–9]. Understanding the chaotic signatures in this transitional regime promotes future technological applications[10–13] emerging at the interface between classical and quantum mechanics realms or, equivalently, ray and wave realms in optical microcavities[1,2,14–16]. Yet, in a more general sense, the level statistics of the microcavity mirror universal behaviors observed in various chaotic physical systems, such as Rydberg atoms[17–19], ultra-cold atoms[20–22], quantum dots[23–25], and many-body systems[26–29].

The boundary deformation (BD) in microcavity has been considered the most common approach for phase space engineering to yield the desired optical properties. The main idea is based on the observation that BD sensitively reconfigures the underlying phase space transportation[30,31]. Alternative approaches also have been proposed, such as tailoring phase space by a defect[32] or including a circular hole inside the cavity[33,34]. Despite these comprehensive efforts, previous approaches still require a holistic device change at the fabrication stage, which remains the main obstacle to further rapid progress. In this regard, developing a new platform on which light dynamics can be studied by in situ experimental control is genuinely appealing. Here, we propose a two-dimensional periodic lattice structure consisting of multiple chaotic microcavities as a promising breakthrough. We reveal that the external crystal momentum coupling to the internal cavity dynamics can take over the role of the BD by breaking and restoring the inherent symmetry of the cavity. Both the direction and the amplitude of the external momentum can be readily controlled by steering the coherent excitation light sources. As a result, cavity lattice systems promise a hold for feasible control of wave chaos features such as dynamical localization and tunneling[35–39].

Correspondence: Hee Chul Park (hc2725@gmail.com) or Moon Jip Park (moonjippark@hanyang.ac.kr)
[1]Center for Theoretical Physics of Complex Systems, Institute for Basic Science (IBS), Daejeon 34126, Republic of Korea
[2]Department of Physics, Pukyong National University, Busan 48513, Republic of Korea
Full list of author information is available at the end of the article
These authors contributed equally: Hee Chul Park, Moon Jip Park

© The Author(s) 2023
Open Access This article is licensed under a Creative Commons Attribution 4.0 International License, which permits use, sharing, adaptation, distribution and reproduction in any medium or format, as long as you give appropriate credit to the original author(s) and the source, provide a link to the Creative Commons license, and indicate if changes were made. The images or other third party material in this article are included in the article's Creative Commons license, unless indicated otherwise in a credit line to the material. If material is not included in the article's Creative Commons license and your intended use is not permitted by statutory regulation or exceeds the permitted use, you will need to obtain permission directly from the copyright holder. To view a copy of this license, visit http://creativecommons.org/licenses/by/4.0/.

In this work, we explore chaotic signatures in periodic lattices dictated by the Bloch theorem for the first time. We study the adiabatic change of the internal cavity states due to the crystal momentum coupling as

$$\Psi_{\text{tot}}(\mathbf{r}) = e^{i\mathbf{k}\cdot\mathbf{r}}\psi_{\text{int}}(\mathbf{r}) \tag{1}$$

where $\Psi_{\text{tot}}(\mathbf{r})$ and $\mathbf{k}$ represent the total wave function over the lattice and the crystalline momentum, respectively. Here, $\psi_{\text{int}}(\mathbf{r})$ describes the internal dynamics of the cavity states, which we focus on. The coupling between the internal phase space dynamics and the crystal momentum is observed explicitly. In particular, the momentum-induced coupling leads to the hybridizations of the wave function from the scar states to the regular orbit states; namely, we observe the crystal momentum-induced *dynamical localization transition* of the internal dynamics. On the lattice scale, we find that introducing the additional deformation leads to the finite Berry curvature and Hall effect triggered by skew scattering events. Our work firstly promotes applications to topological optical transport utilizing chaotic states. Finally, we discuss the possibility of extending our studies to various lattice systems.

We consider a square lattice consisting of a single dielectric cavity with a relative refractive index, $n_{\text{in}}/n_{\text{out}} = 10$, inside the cavity [see Fig. 1]. With this high refractive index, we can find energetically well-isolated target modes by suppressing undesired overlaps with other extra modes. However, our result is generally applicable to the broad range of the refractive index. The boundary of each cavity is determined by the four-fold rotational symmetric (C_4) deformation, which can be represented as, $r(\theta;\varepsilon) = r_0[1-\varepsilon\cos(4\theta)]$, where ε denotes the deformation strength. $r_0 = R/\sqrt{1+\varepsilon^2/2}$, where R is the radius of the circle when $\varepsilon = 0$, is the normalization constant preserving a cavity area under the variation of ε. The Helemholtz equation, $-\nabla^2\vec{\psi} = n^2(x,y)\frac{\omega^2}{c^2}\vec{\psi}$, is solved to obtain resonant frequencies ω of the transverse-magnetic (TM)-polarized modes $[\vec{\psi} = (0,0,E_z)]$, where c is a speed of light. For TM modes, the waves and their normal derivative are set to be continuous across the cavity boundary. The two lattice constants, where we impose a periodic boundary condition accordingly, are given by $|a_x| = |a_y| = a = 2.2R$. To numerically obtain the modes both in a single cavity and a lattice, we implement the boundary element method[40–43].

Under a weak BD, invariant tori in the ray-dynamical phase space of the integrable system are destroyed according to the Kolmogorov-Arnold-Moser (KAM) and Poincaré-Birkhoff theorems[44,45]. As the deformation increases, the regular and chaotic regions fill the phase space before it becomes fully chaotic and ergodic. Figure 2 shows the phase space in the Birkhoff-coordinate $(q/L, p = \sin\chi) \in [0,1]\times[-1,1]$[46]. Here, q/L is the normalized boundary arclength where the ray bounces off (L is a cavity perimeter), and χ is the incident angle of the ray. The mixed phase space in the figure shows the island structures of regular motions surrounded by a chaotic sea. See Supplementary Materials for details.

Results

Two degenerate scar modes[47], the non-trivial localization on the unstable fixed points, are observed in the single cavity case for $\omega R/2\pi c \approx 0.375$ at $\varepsilon = 0.05$. A series of thick blue curves in Fig. 1c show the successive regular and scar modes in which a similar sequence has been analyzed[48]. The scar modes form a pair under the underlying C_4-symmetry. In the lattice, with the identical cavity geometry, the spectra at zero momentum exhibit very similar energy eigenstates (Fig. 1d). We observe the pair of scar modes equally for almost the same energy as the single cavity case. Figure 2a, b shows the Husimi distributions of the two degenerate scar states, which are localized on top of the distinct unstable fixed points. These fixed points correspond to period-2 (i.e., two bounces for one cycle of a classical orbit) unstable periodic orbits shown in the leftmost panels in Fig. 2. The black curves in Fig. 2 show the stable and unstable manifolds of the period-2 unstable orbit, and the unstable fixed points corresponding to this orbit are the crossing points of those manifolds. Note that the Husimi distributions are obtained for the cavity boundary wave, and the inside-incident version was employed[49,50].

We now consider the inclusion of the finite crystal momentum $\mathbf{k} = (k_x, k_y)$. In the presence of the non-zero crystal momentum, we observe the degeneracy lifting of the two scar modes. This lifting indicates the state hybridization due to the C_4-rotational symmetry breaking of the internal wave function with the non-zero momentum. The hybridized states are found to localize prominently around the period-4 bow-tie orbit (see the rightmost panels in Fig. 2), the satellite orbit of the central period-2 island. Figure 2c, d exemplifies the Husimi distributions for these hybridized modes localized on the bow-tie orbits. The mode evolution depending on the crystalline momentum variations in cavity lattices can be equivalently realized in single cavities by applying the additional deformation perturbation. See Supplementary Materials for detailed demonstrations.

In addition, Fig. 3b–e shows the hybridized states that have strong directional anisotropy in the direction of the crystal momentum. To be specific, the hybridization of the two scar modes are numerically obtained and described by the effective Hamiltonian, given as[51],

$$H_{\text{SO}} = \frac{\Delta_{\text{hyb}}}{2}(\cos k_x - \cos k_y)\sigma_x + \text{V}_0 \sin k_x \sin k_y \sigma_z \tag{2}$$

where σ represent the Pauli matrices for the scar state degree of freedom. $\Delta_{\text{hyb}} = 1.156\times10^{-3}$ represents the

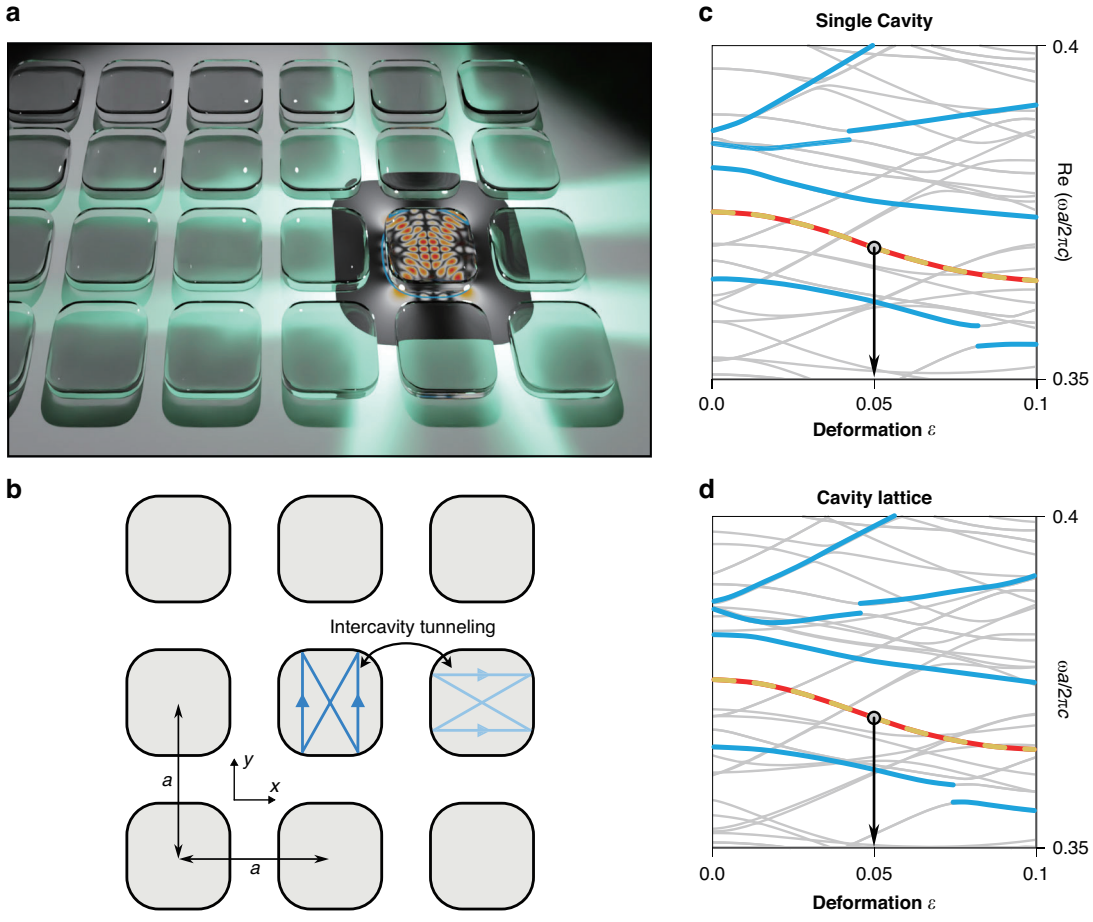

Fig. 1 Bloch theorem dictated scar lattice. a Conceptual illustration of a photonic crystal consisting of a deformed dielectric microcavities. **b** Schematic diagram of a square lattice unit-cell with a lattice constant a. **c** Real part resonant frequencies in a single cavity as a function of the cavity deformation ε. **d** Energy eigenvalues in a cavity array lattice as a function of ε at zero crystalline momentum $\mathbf{k} = 0$ [Γ in Fig. 4a]. In **c** and **d**, successive Demkov-type couplings[56] for the stable regular modes and the scar modes are highlighted by thick curves. The arrows at $\varepsilon = 0.05$ mark the degenerated scar modes (solid and dashed curves) we study

hybridization strength between the two scar modes, while $V_0 = 0.213 \times 10^{-3}$ represents the relative energy shift of the two states, respectively. Since the two scar states are energetically well-decoupled from other states, we can consider the two scar states as the effective spinor ($|\uparrow\rangle$ and $|\downarrow\rangle$). Under this spinor representation, the spinor wind twice around the loop encircling the zero momentum (Fig. 3a). This winding of the spinor gives rise to the 2π-Berry phase: $\gamma \equiv i\oint\langle\psi(\mathbf{k})|\nabla_{\mathbf{k}}|\psi(\mathbf{k})\rangle d\mathbf{k} = 2\pi$, where $|\psi(\mathbf{k})\rangle$ indicates one of the scar states and $i = \sqrt{-1}$. The degeneracy of the spinor scar states manifests as the topological quadratic band touchings (QBT) protected by C_4-symmetry in the momentum space (see Fig. 4a)[52]. Here, the mode hybridization due to the crystalline momentum is not restricted in the scar modes and is valid for the general modes that exhibit a degeneracy at time-reversal invariant momenta.

Maximal momentum coupling

When the momentum becomes maximal near the Brillouin zone (BZ) boundary [$X = (\pi,0)$ and $Y = (0,\pi)$], the wave function characteristics in the whole unit-cell domain deviate significantly due to the change in the boundary condition. For instance, at X point, the internal wave function satisfies the anti-periodic boundary condition on the unit-cell boundary: $\psi_{\mathrm{Int}}(x + a, y) = -\psi_{\mathrm{Int}}(x, y)$ and $\psi_{\mathrm{Int}}(x, y + a) = \psi_{\mathrm{Int}}(x, y)$. The linear combination of the two scar states forms two regular states depending on its parity, [$\psi(x,y) = \pm\psi(-x,y)$], due to C_4-rotational symmetry. At the X point in BZ, there exist only two possibilities that the resonant energy of the regular state can adiabatically deform. First, even parity regular state, $\psi_E(x,y)$ (Fig. 4b), is incompatible with the anti-periodic boundary condition unless the wave function vanishes at the unit-cell boundary. The vanishing wave function manifests as the flat band with zero group velocity (see the

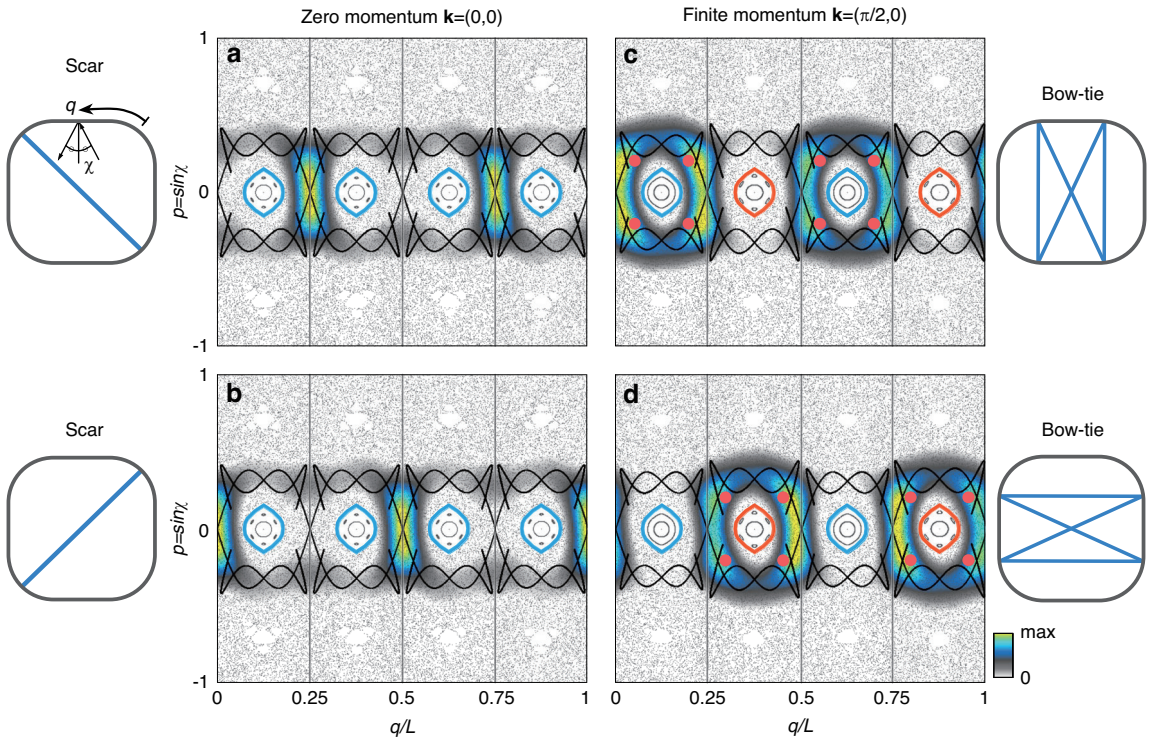

Fig. 2 Phase space of deformed cavity. Husimi functions for modes in a cavity lattice superimposed on the ray-dynamical classical phase space (underlying gray dots) in Birkhoff-coordinate $(q/L, p = \sin\chi)$, where q/L is arclength normalized by a cavity perimeter L and χ an incident angle of ray. In (**a**)–(**d**), the four large closed islands and the crossing points of stable and unstable manifolds (black curves) at $p \sim 0$ correspond to period-2 stable and unstable orbits, respectively. The orange dots in (**c**) and (**d**) represent the phase space points of the bow-tie orbit. **a**, **b** The Husimi distributions for the scar states obtained when $\mathbf{k} = (k_x, k_y) = (0, 0)$, while (**c**) and (**d**) are for the bow-tie orbit states induced by couplings of the two scar states when $\mathbf{k} = (\pi/2, 0)$. The leftmost and rightmost panels show corresponding classical orbits in real space. The four vertical lines in (**a**–**d**) indicate a quarter arclength interval $L/4$. When $\mathbf{k} = (0, 0)$ (**a**, **b**), the phase space (e.g., islands and manifolds) exhibits an $L/4$ translation symmetry, and the Husimi functions in (**a**) and (**b**) are distributed mutually exclusively. On the other hand, when $\mathbf{k} = (\pi/2, 0)$ (**c**, **d**), the translation symmetry of the phase space breaks, and the Husimi distributions in (**c**) and (**d**) have large overlaps around the vertical lines. Detailed correspondences between the Bloch momenta **k** and the phase space deformation can be found in Supplementary Materials. The continuous evolution of the Husimi function and the underlying phase space over the range $[\pi/4 \leqq \arctan(k_y/k_x) \leqq 9\pi/4]$ for $|\mathbf{k}| = \pi/2$ is shown in the supplementary animations: "Ani_supple_phc_hus1_series.mov" and "Ani_supple_phc_hus2_series.mov"

upper band along the X-M interval in Fig. 4a). In addition since $\psi_E(x,y)$ is confined more densely inside the cavity, where the refractive index is higher, the effective wavelength is reduced, i.e., even parity states form higher energy states (point "i" in Fig. 4a).

On the other hand, the odd parity regular state, $\psi_O(x,y)$ (Fig. 4c), shows the compensating intensity enhancement at the unit-cell boundary since the even and odd wave functions must form the complete basis of the two original scar modes. Hence, it results in lengthened effective wavelength (i.e., more waves are outside the cavity, the lower refractive index region) and manifests as the lower energy resonant states (point "ii" in Fig. 4a). Finally, when the momentum vector reaches the BZ corner $[M = (\pi,\pi)]$, the global C_4-rotational symmetry is restored. In this case, the hybridization disappears to form the degenerate QBT again, which can be interpreted as a revived dynamical localization of the spinor scar modes.

Skew boundary scattering in Chaotic states

At last, we consider the scar states in the presence of the generic BD perturbation, which is given as $\delta r(\theta) = \epsilon_1 \cos(N\theta + \phi_0)$. For the even-number oscillating BD $[N \in 2Z]$ [e.g., $(N,\epsilon_1,\phi_0) = (2,0.01,0)$], which preserves C_2 symmetry, the rotational symmetry of the cavity is lowered from C_4 to C_2 symmetry, the topological protection of QBT is lost. Correspondingly, the QBT-carrying 2π-Berry phase can split into a couple of the Dirac linear band crossings, which of each is associated with the π-Berry phase. On the other hand, for odd-number oscillating BD $[N \in 2Z + 1]$, C_2-symmetry breaking induces the skew-symmetric scattering of the chaotic modes [see Fig. 5b], which induces the non-zero Berry curvature $\{\Omega_{xy}(\mathbf{k}) = i[\langle \nabla_{k_x}\psi(\mathbf{k})|\nabla_{k_y}\psi(\mathbf{k})\rangle - (y \leftrightarrow x)]\}$ in the momentum space. Figure 5c shows the calculated Berry curvature for $[(N, \epsilon_1, \phi_0) = (5, 0.01, \frac{\pi}{10})]$. Since the underlying time-reversal symmetry ensures the

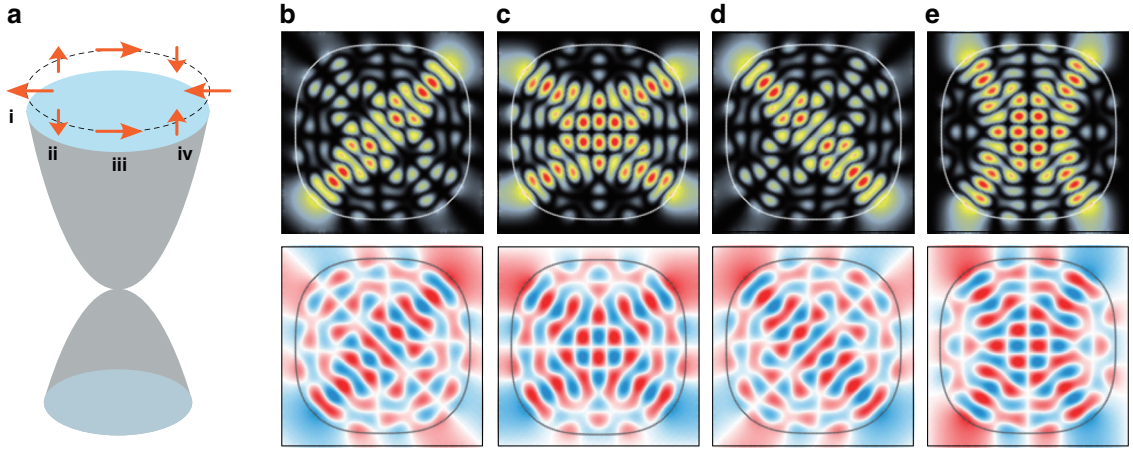

Fig. 3 Coupling between the internal phase space dynamics and the crystal momentum. a Schematic illustration of the pseudo-spin evolution along the encircling around the zero crystalline momentum $(k_x, k_y) = (0, 0)$ (Γ in Fig. 4a). **b**–**e** The upper and lower panels display the square modulus $|\psi|^2$ and the real part Re(ψ) of wave functions corresponding to, respectively, i–iv in (**a**). The directions of the crystalline momentum for (**b**), (**c**), (**d**), and (**e**) are equivalent to the ones of $(k_x, k_y) = (\pi, -\pi), (\pi, 0), (\pi, \pi)$, and$(0, \pi)$, respectively

antisymmetry of the local Berry curvature $\left[\Omega_{xy}(\mathbf{k}) = -\Omega_{xy}(-\mathbf{k})\right]$, the total sum (monopole) of the curvature vanishes. Accordingly, the skew scattering by the BD is characterized by the finite dipole moment of the local Berry curvature[53,54]:

$$D_j = \sum_{\mathbf{k}} \partial_{k_j} \Omega_{xy}(\mathbf{k}) \tag{3}$$

where $j = x,y$.

Since the optical microcavity array can be excited by the coherent beam source with a well-defined incident momentum, the Berry curvature dipole can be measured through the skew-symmetric beam transport. The semi-classical transport equation[55] describes the light dynamics of the Mie regime, and the non-zero Berry dipole manifests as the effective magnetic field as,

$$\mathbf{v}_{\mathbf{k}} = \frac{\partial E_{\mathbf{k}}}{\partial \mathbf{k}} + \dot{\mathbf{k}} \times \Omega_{xy}(\mathbf{k})\hat{z},\ \dot{\mathbf{k}} = \nabla n(\mathbf{r}) \tag{4}$$

where $\mathbf{v}_{\mathbf{k}}$ is the group velocity vector of the scar states having energy $E_{\mathbf{k}}$, and $n(\mathbf{r})$ is the slowly varying local refractive index. The second term $\left(\dot{\mathbf{k}} \times \Omega_{xy}\right)$ in Eq. (4) gives rise to skew-symmetric light transport that can be captured by control of the incident beam momentum $\mathbf{k}$. The explicit demonstration of the skew-symmetric light transportation can be found in Supplementary Materials.

Discussion

To conclude, we have studied the wave chaos of the deformed cavity coupled to the external crystalline momentum in a periodic cavity array. The external crystalline momentum now replaces the role of the boundary shape deformation. By controlling the momentum, we observe the dynamical localization transitions. Our work provides a new promising platform, enabling the in situ study of various wave chaos phenomena. For example, if the additional higher energy and lower energy states are involved, it can induce crystal momentum-induced dynamical tunneling phenomena. This will be the topic of future study.

In addition, we note that, contrary to the previous studies of the topological photonic crystals (which mainly focus on the Rayleigh regime), the governing dynamics of the chaotic state in the Mie regime is described by the semi-classical transport. In this work, we propose, for the first time, the possibility of realizing Berry curvature-induced transport phenomena that utilize the intrinsic wave property of the chaotic states. The crossover between Rayleigh and Mie regime of Berry curvature-induced transport would pioneer a new aspect of wave-particle correspondence in the field of wave chaos.

Our work can be generalized in a few different aspects. Though we have considered the simple square lattice, many other two-dimensional lattices are expected to show qualitatively different behaviors. For instance, away from a simple Bravais lattice, the deformed cavity in Lieb and Kagome lattice is expected to produce a flat band. The intrinsic localization properties would give rise to a stronger coupling within a unit-cell. Further studies on the various lattice systems and wave chaos would also be an intriguing topic for future study.

Methods

We solve the Helmholtz wave equation, which is deduced from Maxwell's equations without sources, for optical modes

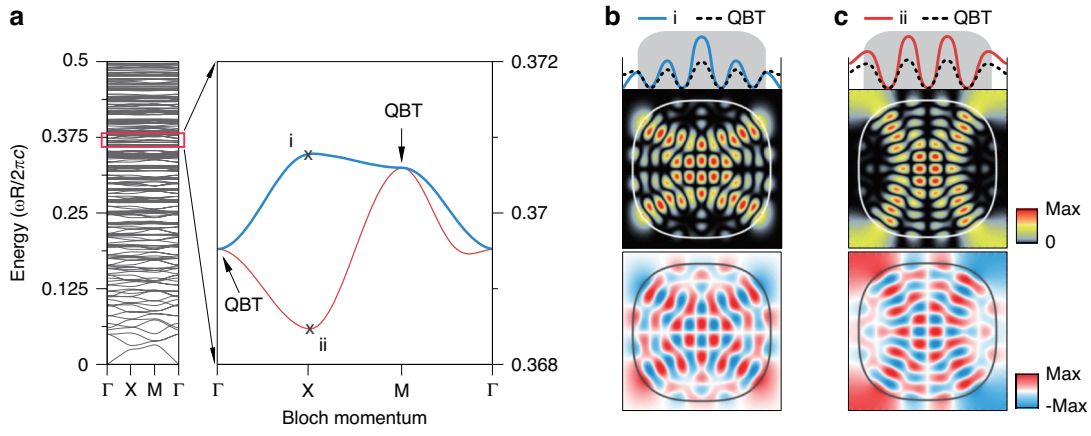

Fig. 4 Band structures and scar modes. a Energy bands as a function of the crystalline momentum (k_x, k_y) for a fixed cavity deformation $\varepsilon = 0.05$. The zoomed bands correspond to the ones indicated by the arrow in Fig. 1d. **b** Spatial distribution of the even parity mode (ψ_E) in a unit-cell for $(k_x, k_y) = (\pi, 0)$ (*i* in **a**). The upper panel depicts the wave projection onto the *x*-axis showing the vanished wave at the unit-cell boundary and the dense confinement of the wave inside the cavity region (shaded rectangle). **c** The same as (**b**) but for the odd parity mode (ψ_O) (*ii* in **a**). The upper panel depicts the intense wave distribution outside the cavity, including the unit-cell boundary

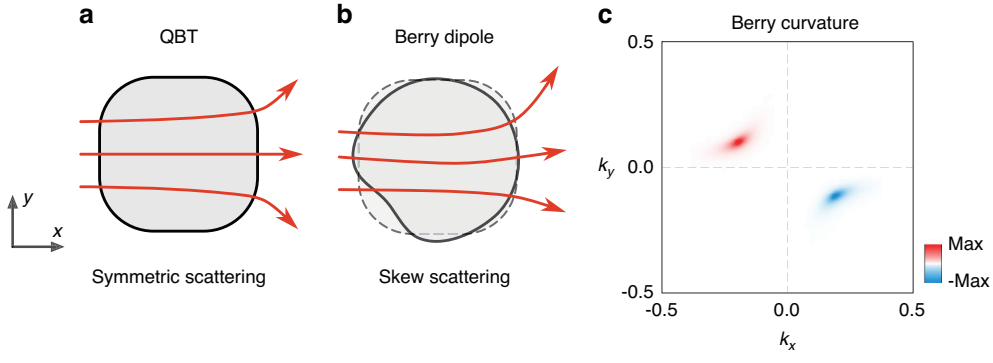

Fig. 5 Skew scattering due to the Berry curvature. Schematic illustration of BDs. **a** Original C_4-symmetric boundary with QBT and **b** C_4-breaking boundary. C_4-breaking boundary perturbation splits the single QBT into a pair of Dirac cones. Subsequently, C_2-breaking boundary perturbation gaps out the Dirac cones and induces the Berry curvature dipole. The Berry curvature dipole induces the skew scattering depending on the incident momentum, k_{inc}. **c** Distribution of non-zero Berry curvature in the momentum space induced by scar states

in single cavities and photonic crystals,

$$-\nabla^2\vec{\psi} = n^2(\mathbf{r})\frac{\omega^2}{c^2}\vec{\psi} \tag{5}$$

where $n(\mathbf{r})$ and $\omega = ck$ are, respectively, the refractive index of the piecewise homogeneous medium and the free-space temporal frequency with vacuum wavenumber k and speed of light c. Given the cavity boundary shape, $R(\theta;\varepsilon) = R_0[1 - \varepsilon\cos(4\theta)]$, where $R_0 = \rho/\sqrt{1+\varepsilon^2/2}$, we set $n(\mathbf{r}) = 10$ for $|\mathbf{r}| < R(\theta;\varepsilon)$ and $n(\mathbf{r}) = 1$ otherwise. ρ is the radius of a circle when $\varepsilon = 0$. The lattice constant is given as $|a_x| = |a_y| = a = 2.2\rho$. We focus on the transverse magnetic [TM; $\vec{\psi} = (0, 0, E_z)$] polarization of modes. The TM-polarized modes fulfill the dielectric boundary condition that E_z and are continuous across the boundary interface of two different refractive index domains. Here, $\vec{\nu}$ is an outward normal vector of the boundary. Note that the transverse-electric [TE; $\vec{\psi} = (0, 0, H_z)$] modes satisfy a different boundary condition: H_z and are continuous, yet, still the solution of the same wave equation, Eq. (5). In addition to the dielectric boundary conditions, we impose a two-dimensional periodic condition at the unit cell boundary of the two-dimensional periodic lattice. A pure outgoing wave condition at infinity is applied for the modes in the single cavities. To solve Eq. (5) numerically, we employ the boundary element method (BEM)[40,41] and further implement the block Sakurai–Sugiura method[42,43] to compute the optical modes more efficiently.

Acknowledgements
We acknowledge financial support from the Institute for Basic Science (IBS) in the Republic of Korea through the project IBS-R024-D1. This work is also supported by the research fund of Hanyang University (HY-202300000001149).

Author details
[1]Center for Theoretical Physics of Complex Systems, Institute for Basic Science (IBS), Daejeon 34126, Republic of Korea. [2]Department of Physics, Pukyong National University, Busan 48513, Republic of Korea. [3]Department of Physics, Hanyang University, Seoul 04763, Republic of Korea

Author contributions
All authors of C.H.Y., H.C.P., and M.J.P. contributed to this project by proposing the idea, initiating this project, collecting numerical data, analyzing numerical data, and carrying out mathematical analysis. All authors commented on and wrote the manuscript draft.

Conflict of interest
The authors declare no competing interests.

Supplementary information The online version contains supplementary material available at https://doi.org/10.1038/s41377-023-01156-9.

Received: 22 November 2022 Revised: 27 March 2023 Accepted: 12 April 2023
Published online: 04 May 2023

References

1. Cao, H. & Wiersig, J. Dielectric microcavities: model systems for wave chaos and non-Hermitian physics. *Rev. Mod. Phys.* **87**, 61–111 (2015).
2. Nöckel, J. U. & Stone, A. D. Ray and wave chaos in asymmetric resonant optical cavities. *Nature* **385**, 45–47 (1997).
3. Yi, C. H., Kullig, J. & Wiersig, J. Pair of exceptional points in a microdisk cavity under an extremely weak deformation. *Phys. Rev. Lett.* **120**, 093902 (2018).
4. Kullig, J., Yi, C. H. & Wiersig, J. Exceptional points by coupling of modes with different angular momenta in deformed microdisks: a perturbative analysis. *Phys. Rev. A* **98**, 023851 (2018).
5. Kullig, J. & Wiersig, J. Microdisk cavities with a Brewster notch. *Phys. Rev. Res.* **3**, 023202 (2021).
6. Wiersig, J. Structure of whispering-gallery modes in optical microdisks perturbed by nanoparticles. *Phys. Rev. A* **84**, 063828 (2011).
7. Stöckmann, H. J. *Quantum Chaos: An Introduction* (Cambridge University Press, 2007).
8. Haake, F. *Quantum Signatures of Chaos*. 3rd edn (Springer, 2010).
9. Casati, G., Guarneri, I. & Smilansky, U. *Quantum Chaos* (Elsevier, 1993).
10. Jiang, X. F. et al. Chaos-assisted broadband momentum transformation in optical microresonators. *Science* **358**, 344–347 (2017).
11. Bittner, S. et al. Suppressing spatiotemporal lasing instabilities with wave-chaotic microcavities. *Science* **361**, 1225–1231 (2018).
12. Yang, L. Fighting chaos with chaos in lasers. *Science* **361**, 1201 (2018).
13. Chen, L. K. et al. Regular-orbit-engineered chaotic photon transport in mixed phase space. *Phys. Rev. Lett.* **123**, 173903 (2019).
14. Harayama, T. et al. Asymmetric stationary lasing patterns in 2D symmetric microcavities. *Phys. Rev. Lett.* **91**, 073903 (2003).
15. Shinohara, S. et al. Chaos-assisted directional light emission from microcavity lasers. *Phys. Rev. Lett.* **104**, 163902 (2010).
16. Sunada, S. et al. Signature of wave chaos in spectral characteristics of microcavity lasers. *Phys. Rev. Lett.* **116**, 203903 (2016).
17. Aßmann, M. et al. Quantum chaos and breaking of all anti-unitary symmetries in Rydberg excitons. *Nat. Mater.* **15**, 741–745 (2016).
18. Hunter, A. L. et al. Rydberg composites. *Phys. Rev. X* **10**, 031046 (2020).
19. Facon, A. et al. A sensitive electrometer based on a Rydberg atom in a Schrödinger-cat state. *Nature* **535**, 262–265 (2016).
20. Arnal, M. et al. Chaos-assisted tunneling resonances in a synthetic Floquet superlattice. *Sci. Adv.* **6**, eabc4886 (2020).
21. Frisch, A. et al. Ultracold dipolar molecules composed of strongly magnetic atoms. *Phys. Rev. Lett.* **115**, 203201 (2015).
22. Frisch, A. et al. Quantum chaos in ultracold collisions of gas-phase erbium atoms. *Nature* **507**, 475–479 (2014).
23. Ponomarenko, L. A. et al. Chaotic Dirac billiard in graphene quantum dots. *Science* **320**, 356–358 (2008).
24. Albert, F. et al. Observing chaos for quantum-dot microlasers with external feedback. *Nat. Commun.* **2**, 366 (2011).
25. Moore, F. L. et al. Observation of dynamical localization in atomic momentum transfer: a new testing ground for quantum chaos. *Phys. Rev. Lett.* **73**, 2974–2977 (1994).
26. Sá, L., Ribeiro, P. & Prosen, T. Complex spacing ratios: a signature of dissipative quantum chaos. *Phys. Rev. X* **10**, 021019 (2020).
27. Pandey, M. et al. Adiabatic eigenstate deformations as a sensitive probe for quantum chaos. *Phys. Rev. X* **10**, 041017 (2020).
28. Friedman, A. J. et al. Spectral statistics and many-body quantum chaos with conserved charge. *Phys. Rev. Lett.* **123**, 210603 (2019).
29. Dahan, D., Arwas, G. & Grosfeld, E. Classical and quantum chaos in chirally-driven, dissipative Bose-Hubbard systems. *npj Quantum Inf.* **8**, 14 (2022).
30. Wiersig, J. & Hentschel, M. Combining directional light output and ultralow loss in deformed microdisks. *Phys. Rev. Lett.* **100**, 033901 (2008).
31. Shim, J. B. et al. Uncertainty-limited turnstile transport in deformed microcavities. *Phys. Rev. Lett.* **100**, 174102 (2008).
32. Qian, Y. J. et al. Regulated photon transport in chaotic microcavities by tailoring phase space. *Phys. Rev. Lett.* **127**, 273902 (2021).
33. Wiersig, J. & Hentschel, M. Unidirectional light emission from high-*Q* modes in optical microcavities. *Phys. Rev. A* **73**, 031802(R) (2006).
34. Bäcker, A. et al. Quality factors and dynamical tunneling in annular microcavities. *Phys. Rev. A* **79**, 063804 (2009).
35. Davis, M. J. & Heller, E. J. Quantum dynamical tunneling in bound states. *J. Chem. Phys.* **75**, 246–254 (1981).
36. Keshavamurthy, S. & Schlagheck, P. *Dynamical Tunneling: Theory and Experiment* (Taylor & Francis, 2011).
37. Bäcker, A. et al. Dynamical tunneling in mushroom billiards. *Phys. Rev. Lett.* **100**, 174103 (2008).
38. Guarneri, I., Casati, G. & Karle, V. Classical dynamical localization. *Phys. Rev. Lett.* **113**, 174101 (2014).
39. Bitter, M. & Milner, V. Experimental observation of dynamical localization in laser-kicked molecular rotors. *Phys. Rev. Lett.* **117**, 144104 (2016).
40. Wiersig, J. Boundary element method for resonances in dielectric microcavities. *J. Opt. A: Pure Appl. Opt.* **5**, 53–60 (2003).
41. Veble, G., Prosen, T. & Robnik, M. Expanded boundary integral method and chaotic time-reversal doublets in quantum billiards. *N. J. Phys.* **9**, 15 (2007).
42. Sakurai, T., Futamura, Y. & Tadano, H. Efficient parameter estimation and implementation of a contour integral-based eigensolver. *J. Algorithms Comput. Technol.* **7**, 249–269 (2013).
43. Isakari, H., Takahashi, T. & Matsumoto, T. Periodic band structure calculation by the Sakurai–Sugiura method with a fast direct solver for the boundary element method with the fast multipole representation. *Eng. Anal. Bound. Elem.* **68**, 42–53 (2016).
44. Tabor, M. *Chaos and Integrability in Nonlinear Dynamics: An Introduction* (Wiley-Interscience, 1989).
45. Strogatz, S. H. *Nonlinear Dynamics and Chaos: With Applications to Physics, Biology, Chemistry, and Engineering*. 2nd edn (CRC Press, 2018).
46. Birkhoff, G. D. On the periodic motions of dynamical systems. *Acta Math.* **50**, 359–379 (1927).
47. Heller, E. J. Bound-state eigenfunctions of classically chaotic Hamiltonian systems: scars of periodic orbits. *Phys. Rev. Lett.* **53**, 1515–1518 (1984).
48. Yi, C. H. et al. Separatrix modes in weakly deformed microdisk cavities. *Opt. Express* **25**, 8048–8062 (2017).
49. Hentschel, M., Schomerus, H. & Schubert, R. Husimi functions at dielectric interfaces: Inside-outside duality for optical systems and beyond. *Europhys. Lett.* **62**, 636–642 (2003).
50. Kim, I. et al. Husimi functions at gradient index cavities designed by conformal transformation optics. *Opt. Express* **26**, 6851–6859 (2018).
51. Yi, C. H., Park, H. C. & Park, M. J. Strong interlayer coupling and stable topological flat bands in twisted bilayer photonic moiré superlattices. *Light Sci. Appl.* **11**, 289 (2022).
52. Sun, K. et al. Topological insulators and nematic phases from spontaneous symmetry breaking in 2d fermi systems with a quadratic band crossing. *Phys. Rev. Lett.* **103**, 046811 (2009).
53. Sodemann, I. & Fu, L. Quantum nonlinear hall effect induced by berry curvature dipole in time-reversal invariant materials. *Phys. Rev. Lett.* **115**, 216806 (2015).
54. Xiao, D., Chang, M. C. & Niu, Q. Berry phase effects on electronic properties. *Rev. Mod. Phys.* **82**, 1959–2007 (2010).
55. Nagaosa, N. et al. Anomalous Hall effect. *Rev. Mod. Phys.* **82**, 1539–1592 (2010).
56. Demkov, Y. N. & Osherov, V. I. Stationary and nonstationary problems in quantum mechanics that can be solved by means of contour integration. *Sov. Phys. JETP* **26**, 916–921 (1968).